Green Chemistry

PAPER

View Article Online
View Journal | View Issue

Cite this: *Green Chem.*, 2017, **19**, 3014

MoO_3–TiO_2 synergy in oxidative dehydrogenation of lactic acid to pyruvic acid†

Kaituo Liu,[a] Xiaoming Huang,[a] Evgeny A. Pidko *[a,b] and Emiel J. M. Hensen *[a]

An efficient catalytic process for the oxidative dehydrogenation of biomass-derived lactic acid by earth-abundant MoO_3/TiO_2 mixed oxide catalysts is presented. A series of MoO_3/TiO_2 materials with varied MoO_3 loadings were prepared and their performance in the aerobic and anaerobic conversion of lactic acid was evaluated. A strong synergistic effect between MoO_3 and TiO_2 components of the mixed oxide catalyst was observed. Optimum catalysts in terms of activity and pyruvic acid selectivity can be obtained by ensuring a high dispersion of MoO_x species on the titania surface. Mo-oxide aggregates catalyze undesired side-reactions. XPS measurements indicate that the redox processes involving supported Mo ions are crucial for the catalytic cycle. A mechanism is proposed, in which lactic acid adsorbs onto basic sites of the titania surface and is dehydrogenated over the Mo=O acid–base pair of a vicinal tetrahedral Mo site. The catalytic cycle closes by hydrolysis of surface pyruvate and water desorption accompanied by the reduction of the Mo center, which is finally oxidized by O_2 to regenerate the initial active site. Under anaerobic conditions, a less efficient catalytic cycle is established involving a bimolecular hydrogen transfer mechanism, selectively yielding propionic and pyruvic acids as the major products. The optimum catalyst is 2 wt% MoO_3/TiO_2 predominantly containing tetrahedral Mo species. With this catalyst the oxidative conversion of lactic acid at 200 °C proceeds with a selectivity of *ca*. 80% to pyruvic acid. The pyruvic acid productivity is 0.56 g g^{-1} h^{-1}.

Received 15th March 2017,
Accepted 4th May 2017

DOI: 10.1039/c7gc00807d

rsc.li/greenchem

1. Introduction

The development of novel catalytic technologies for the efficient production of chemicals and fuels from renewable resources is pivotal for transition to a greener chemical industry. Especially, lignocellulosic biomass is an attractive source of renewable carbon. Novel processes will hinge on the availability of platform molecules, which can be efficiently obtained from biomass and converted into a range of chemical intermediates and end-products.[1,2] Lactic acid (LA) is a prominent platform molecule, which is typically obtained by enzymatic conversion of sugars.[3,4] Scheme 1 depicts the large number of chemical products that can be obtained from LA. Catalytic dehydrogenation of LA to pyruvic acid (PyA) is of considerable importance for the production of L-amino acids,[5] cyanoacrylate adhesives,[6] perfumes, food additives, dietary and weight-control supplements, nutraceuticals, antioxidants[7] and photo-resistant solvents for electronic processing.[8]

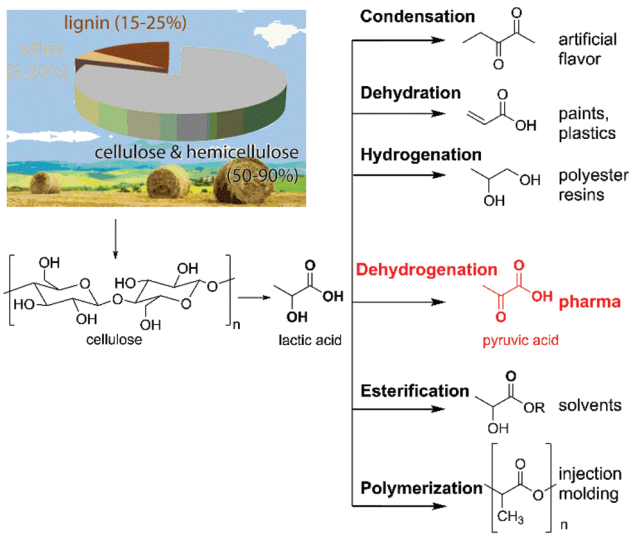

Scheme 1 Potential valorization paths for biomass-derived lactic acid.

The current industrial process for the production of PyA involves the stoichiometric dehydrative decarboxylation of tartaric acid. This approach was originally described by Erlenmeyer in 1881.[9,10] A more sustainable alternative is desir-

[a]*Inorganic Materials Chemistry Group, Schuit Institute of Catalysis, Eindhoven University of Technology, P.O. Box 513, 5600 MB Eindhoven, The Netherlands. E-mail: e.a.pidko@tue.nl, e.j.m.hensen@tue.nl*
[b]*ITMO University, Lomonosova str. 9, St. Petersburg 191002, Russia*
†Electronic supplementary information (ESI) available. See DOI: 10.1039/c7gc00807d

able in order to avoid the formation of large amounts of inorganic waste and to improve the atom efficiency. A challenge in developing direct oxidative dehydrogenation of lactic acid is the high reactivity of PyA. Decarboxylation as well as overoxidation of PyA lowers product selectivity, which is especially a problem at the elevated temperatures necessary to achieve an appreciable reaction rate.[11] The use of lower reaction temperatures usually results in rapid catalyst deactivation due to the blocking of the catalytic surface by oligomers of LA.[3] Phosphate-based catalysts,[11,12] usually containing transition metal promoters,[13] are currently the benchmark systems for oxidative dehydrogenation of LA and its alkylated derivatives. Ai *et al.* described an iron phosphate catalyst for the gas-phase oxidation of LA, which gave a maximum PyA yield of 50% (66% PyA selectivity at 76% LA conversion) at 260 °C.[11] Doping this catalyst with Mo strongly enhanced the catalytic performance and a nearly similar yield of 52% could be achieved already at 200 °C.[12]

Reducible metal oxides represent another important class of promising catalysts for oxidative dehydrogenation of LA. Their acid-based properties strongly affect PyA selectivity. TiO_2, ZrO_2, and SnO_2 typically result in higher selectivity to pyruvates compared to conventional oxidation catalysts such as MoO_3,[14–17] TeO_2,[17] and V_2O_5.[14,18] Rothenberg and co-workers evaluated the activity of a wide range of metal oxides including Fe_2O_3, V_2O_5/MgO–Al_2O_3, ZrO_2, TiO_2, CeO_2, and ZnO for the oxidative dehydrogenation of ethyl lactate.[19] TiO_2 showed superior catalytic performance, reaching up to 75% ethyl pyruvate selectivity at 80% conversion of ethyl lactate. The unique reactivity of TiO_2 is attributed to specific surface sites that selectively activate the hydroxyl group in the reactant.[20] The catalytic properties of these oxides can be further improved by the addition of other metal oxides. The properties of binary oxides such as surface area, acidity, and redox behaviour are often quite different from their single-oxide constituents. A previous study demonstrated the utility of Ni–Nb–O mixed oxides to catalyze oxidative dehydrogenation of LA.[21] PyA yields of up to 18% were obtained at 280 °C. Binary oxides containing Mo, *e.g.*, Fe_2O_3–MoO_3, and TeO_2–MoO_3, have also been reported as active catalysts for the dehydrogenation of LA or ethyl lactate. For these catalysts, lactate conversions of 75% with pyruvate selectivities higher than 90% have been reported.[22]

In this study we investigated the catalytic performance of heterogeneous MoO_3–TiO_2 (anatase) catalysts for the oxidative dehydrogenation of lactic acid to pyruvic acid. Titania-supported MoO_3 constitutes an important class of catalytic materials showing promising performance in the oxidation of methanol,[23,24] the oxidative dehydrogenation of ethane,[25] propane,[26,27] 1-butene, and *o*-xylene[28] as well as in the hydrodeoxygenation of *m*-cresol.[29] The high catalytic performance of these catalysts in selective oxidation of organic molecules has been linked to highly reactive sites at the interface between the two oxides.[30,31] Accordingly, it has been proposed that the catalytic performance of such materials crucially depends on the dispersion of the MoO_3 phase on TiO_2.[32,33] The formation of the binary system has been shown to be crucial for the activity in alcohol dehydrogenation.[34] It has also been reported that higher MoO_3 dispersion can be achieved using anatase as a catalyst support instead of the rutile TiO_2 phase.[35]

The present work introduces MoO_3, TiO_2 and their mixtures as promising catalysts for obtaining pyruvic acid from lactic acid. The surface properties of the metal oxides were extensively investigated to understand the relationship between the structure and acidic properties and catalytic performance. A mechanism is proposed for the strong synergy observed between isolated tetrahedral Mo-oxide species and the titania support.

2. Experimental

2.1 Materials

TiO_2 (anatase, powder, −325 mesh, ≥99% trace metals basis) and $(NH_4)_6Mo_7O_{24}{\cdot}4H_2O$ (≥99%) were purchased from Sigma-Aldrich. Lactic acid (90%, Sigma-Aldrich), pyruvic acid (98%, Aldrich), acetaldehyde (≥99.5%, Aldrich), methylsuccinic anhydride (98%, Aldrich), propionic acid (≥99.5%, Aldrich), acetic acid (≥99.85%, Aldrich) and citraconic anhydride (98%, Aldrich) were used as received without further purification.

2.2 Catalyst preparation

Two methods were used to synthesize the catalysts, namely physical mixing of the two oxides and wet impregnation of ammonium heptamolybdate on titania. A TiO_2–MoO_3 catalyst was prepared by thoroughly mixing MoO_3 and TiO_2 in a 1 : 2 molar ratio of TiO_2 : MoO_3 with a small amount of water. The resulting paste was spread over a glass plate, dried overnight at 80 °C, crushed, and calcined at 500 °C in air for 6 h. To prepare MoO_3/TiO_2, with MoO_3 loadings in the 1–10 wt% range, an appropriate amount of $(NH_4)_6Mo_7O_{24}{\cdot}4H_2O$ was completely dissolved in deionized water under vigorous stirring for 2 h at room temperature. Then, an appropriate amount of TiO_2 was added to the solution and stirred for 4 h at room temperature. Afterwards, the water was removed under reduced pressure and the resulting solid was dried at 110 °C for 16 h before being calcined at 500 °C for 6 h in static air. A typical procedure for obtaining 5 g of 10 wt% MoO_3/TiO_2 catalyst is as follows: 0.6132 g $(NH_4)_6Mo_7O_{24}{\cdot}4H_2O$ was dissolved in 15 mL deionized water under vigorous stirring followed by addition of 4.5 g TiO_2. Catalysts prepared by wet impregnation are denoted as MT*x*, where *x* represents the weight loading of MoO_3.

2.3 Characterization

Powder X-ray diffraction (XRD) patterns were measured on a Bruker D4 Endeavor powder diffraction system using Cu Kα radiation (40 kV and 30 mA) with a scanning speed of 0.01° min^{-1} in the range of $5° \leq 2\theta \leq 80°$. Scanning electron microscopy (SEM) measurements were performed using a Philips environmental scanning electron microscope FEIXL-30 ESEM FEG in high vacuum mode at low voltage. Textural

analysis was done by nitrogen physisorption on a Tristar 3000 automated gas adsorption system. The samples were degassed at 300 °C for 6 h prior to analysis. Raman spectra were recorded using a Jobin-Yvon T64000 triple-stage instrument at a spectral resolution of 2 cm^{-1}. The excitation laser line at 600 nm was produced by a Kimmon He–Cd laser. The power of the laser was 4 mW. Diffuse reflectance UV-Vis spectra were recorded on a Shimadzu UV-2401 PC spectrometer in a diffuse-reflectance mode using an integrating sphere (internal diameter 60 mm) and $BaSO_4$ was used as the reference. Fourier Transform Infrared (FT-IR) spectra were recorded on a Bruker Vertex V70v FTIR spectrometer in transmission mode. Typically, a powdered sample was pressed into a self-supporting wafer with a density of about 10 mg cm^{-2} and placed inside a controlled environment infrared transmission cell, capable of heating and cooling, gas dosing and evacuation. After calcining the catalyst wafer at 500 °C, the catalyst was evacuated to a pressure better than 2×10^{-5} mbar and the temperature was lowered to 150 °C. A background was recorded. Pyridine was introduced into the cell from a glass ampoule. The sample was then exposed to pyridine at 150 °C for 30 min. After removing physisorbed pyridine by evacuation at 150 °C for 1 h, a spectrum was recorded. Additional spectra were recorded at 150 °C after outgassing at 200 °C and 400 °C for 1 h.

X-ray photoelectron spectroscopy (XPS) measurements were performed using a Thermo Scientific K-Alpha spectrometer, equipped with a monochromatic small-spot X-ray source and a 180° double focusing hemispherical analyzer with a 128-channel detector. Spectra were obtained using an aluminum anode (Al Kα = 1486.6 eV) operating at 72 W and a spot size of 400 μm. Survey scans were measured at a constant pass energy of 200 eV and region scans at 50 eV. The background pressure was 2×10^{-9} mbar and it was 3×10^{-7} mbar Ar during measurement because of the charge compensation dual beam source. Data analysis was performed using Casa XPS software. The binding energy was corrected for surface charging by taking the C 1s peak of adventitious carbon as a reference at 284.5 eV.

Temperature programmed reduction (TPR) experiments were carried out in flow apparatus equipped with a fixed-bed reactor, a computer-controlled oven and a thermal conductivity detector. Typically, 50 mg catalyst was loaded in a tubular quartz reactor. The sample was reduced in 4 vol% H_2 in N_2 at a flow rate of 8 ml min^{-1} whilst heating from room temperature up to 800 °C at a ramp rate of 10 °C min^{-1}. The H_2 signal was calibrated using a CuO/SiO_2 reference catalyst.

2.4 Catalyst activity measurements

2.4.1 Oxidative dehydrogenation of lactic acid. Catalytic tests were performed under atmospheric pressure in a gas phase down-flow fixed-bed reactor (stainless steel, 6 mm inner diameter, 150 mm length). In a typical experiment, 0.3 g of catalyst powder (125–250 μm) were loaded into the reactor and the bed was fixed between quartz wool. The aqueous LA solution (20 wt%) was fed using an HPLC pump at a flow-rate of 0.05 ml min^{-1} to the entry point of the reactor system, where it was vaporized at 190 °C and diluted with air (30 ml min^{-1} STP, STP = standard pressure and temperature). The feed molar LA : H_2O : air composition was 0.6 : 13.3 : 1. The liquid solution fed by the HPLC was prepared by dissolving an appropriate amount of lactic acid (90%, Sigma Aldrich) in deionized water. The reaction temperature was 200 °C. The products were collected in a cold trap installed after the reactor and analyzed by HPLC and GC-FID. The feed concentration and the reaction conditions were selected to ensure a complete vaporization of the LA substrate. HPLC analysis of concentrations of LA, pyruvic acid and acetic acid was carried out on a Shimadzu setup equipped with a UV detector and a Prevail Organic Acid 3u column (Grace, 2.1 × 100 mm column). HPLC analysis was done at room temperature with 25 mM phosphate buffer of pH = 2 as a mobile phase at a flow rate of 0.125 ml min^{-1} and the products were detected using a UV detector. GC-FID analysis was used to quantify acetaldehyde and other hydrocarbon products. The analysis was carried out using a Thermo GC equipped with a Stabilwax-DA capillary column, 30 m × 0.53 mm × 1.0 μm and a flame ionization detector (FID). The oven was set at 40 °C, using a hold time of 5 min, before increasing with a rate of 10 °C min^{-1} to reach 240 °C, followed by another hold time of 20 min. Injector and detector temperatures were 250 °C. For HPLC and GC-FID analysis, the products were quantified using external calibration curves generated with authentic compound solutions (see the ESI†).

The conversion of LA (X) was calculated as

$$X(\%) = \frac{C_{LA,0} - C_{LA}}{C_{LA,0}} \times 100\%$$

The (carbon-based) selectivity of product i was calculated as

$$S_i(\%) = \frac{C_{\text{product } i} \times \text{number of carbon atoms in product } i}{C_{LA,0} \times X \times 3} \times 100\%$$

where $C_{LA,0}$, C_{LA} and $C_{\text{product } i}$ are the concentrations of LA in the feed and after the reactor and the concentration of product i after the reactor, respectively.

2.4.2 Oxidative dehydrogenation of ethanol. Oxidative dehydrogenation of ethanol was carried out in a fixed-bed plug flow reactor system. In a typical experiment, 100 mg of catalyst (sieve fraction 125–250 μm) diluted with 300 mg of α-Al_2O_3 was loaded into a stainless-steel reactor with an internal diameter of 6 mm. Prior to the reaction, the catalyst was stabilized in a mixture of 20 vol% O_2 in N_2 at 300 °C for 4 h. The volumetric composition of the feed mixtures was ethanol : O_2 : He = 1.5 : 4.5 : 94. The reactant feed mixture was obtained by evaporating ethanol in a He flow in a controlled evaporator mixer. All tubings were kept above 120 °C to avoid condensation of the reactants and products. The total gas flow rate was 167 mL min^{-1} with an ethanol flow rate of 2.5 mL min^{-1} (1.5 vol%) and a GHSV of 100 000 mL g_{cat}^{-1} h^{-1} for all experiments. The reactor effluent was analyzed by online gas chromatography (Interscience GC-8000 Top, permanent gases

on the Schincarbon ST80/100 packed column connected to a TCD and hydrocarbons on a Rtx-Wax column connected to an FID). The ethanol conversion (X) and acetaldehyde selectivity (S) were calculated as:

$$X(\%) = \frac{C_{\mathrm{EtOH},0} - C_{\mathrm{EtOH}}}{C_{\mathrm{EtOH},0}} \times 100\%$$

$$S(\%) = \frac{C_{\text{ acetaldehyde}}}{C_{\mathrm{EtOH},0} \times X} \times 100\%$$

3. Results and discussion

3.1. Oxidative dehydrogenation of LA using TiO_2, MoO_3 and their physical mixture

As the starting point of this study, we evaluated the catalytic performance of TiO_2 and MoO_3 catalysts for the oxidative dehydrogenation of LA in continuous flow at an air pressure of 1 bar. LA was fed to the reactor as a 20 wt% aqueous solution. The reaction temperature was 200 °C. The results are shown in Fig. 1. For MoO_3 and TiO_2, stable but low conversion of LA was observed with a relatively high PyA selectivity (~80%). The product distribution is slightly different between these two bulk oxide catalysts. Whereas methylsuccinic anhydride and propionic acid are the major by-products with TiO_2, products of decarboxylation such as acetaldehyde and CO_2 were observed when MoO_3 was used as the catalyst. The decarboxylation by-products decreased with time on stream, suggesting that some highly reactive sites on the MoO_3 surface slowly deactivated. The other by-products included acetic acid, propionic acid and citraconic anhydride formed with selectivities below 1%. The reaction outcome changed drastically when a physical mixture of the two oxides was employed as the catalyst (Fig. 1c). The LA conversion was about three times higher than that for the single component oxides. A steady state was obtained after 3 hours on stream. During the initial transient, the PyA selectivity increased from 61% to 82%, the final selectivity level being similar to that of the much less active single-component catalysts. The decrease in LA conversion was relatively minor. The increase in PyA selectivity was accompanied by lowered formation rates of decarboxylation products CO_2 and acetaldehyde and the overoxidation product acetic acid. When 2 wt% Mo on TiO_2 (MT2) prepared by wet impregnation was employed as the catalyst, higher activity and selectivity with similar stability to the physically mixed catalyst was observed (Fig. 1d). Notably, the selectivity to the decarboxylation products acetaldehyde and carbon dioxide and the overoxidation product acetic acid became lower with time on stream. It should be noted that the amount of carbon dioxide was nearly equal to the amount of acetaldehyde, indicating that carbon dioxide was the product of decarboxylation of lactic acid and not from full combustion reactions. These results clearly demonstrate the synergy between TiO_2 and MoO_3 for the oxidative dehydrogenation of LA.

3.2. Supported MoO_3/TiO_2 catalysts

We investigated further the synergy between MoO_3 and TiO_2 in the oxidative dehydrogenation of LA by evaluating the performance of a series of MoO_3/TiO_2 catalysts with varying MoO_3 loadings (1, 2, 5, 8 and 10 wt%). The catalytic performance of these catalysts after a reaction time of 4 h is shown in Fig. 2. These data further emphasize the synergy between the two oxides. Within this series, the highest LA conversion occurred with the catalyst with the highest MoO_3 loading (MT10). However, its high activity was accompanied by a significant contribution of products of decarboxylation and further oxidation of acetaldehyde to acetic acid. For MT10, the acetic acid selectivity was higher than the PyA selectivity. Lowering the

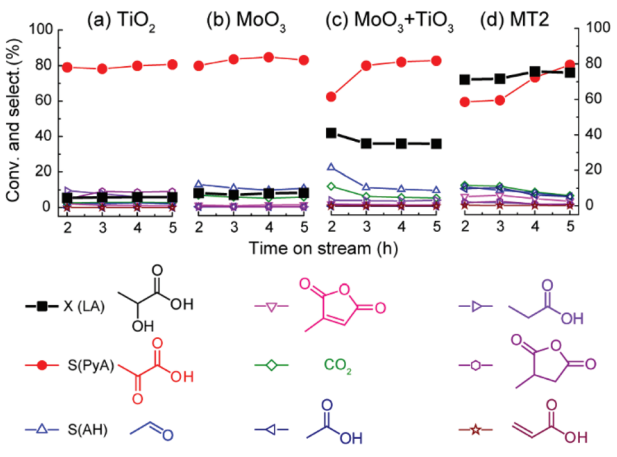

Fig. 1 The evolution of LA conversion (X(LA), %, black squares) and selectivities (S, %) to PyA (S_{PyA}(%), red circles) and other minor products (open symbols) in the presence of 1 bar air over (a) TiO_2, (b) MoO_3, (c) physical mixture of TiO_2 and MoO_3 with a molar ratio of 1 : 2 and (d) the MT2 binary catalyst (conditions: T = 200 °C, p = 1 atm, 4.0 vol% LA, 6.7 vol% air, WHSV = 10 h^{-1}).

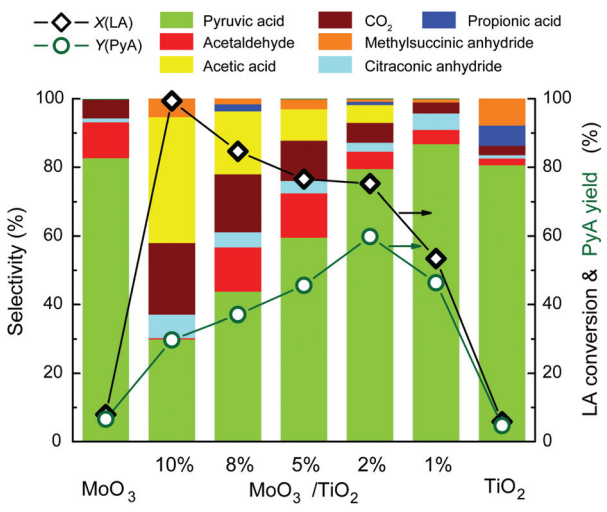

Fig. 2 An overview of LA conversion and PyA yields (respectively, X(LA), ◊ and Y(PyA), ○, %, right axes), and selectivities (bars, left axes) at a 4 h reaction time over TiO_2, MoO_3, and binary molybdena-titania catalysts with varying MoO_3 loadings (conditions: T = 200 °C, p = 1 atm, 4.0 vol% LA, 6.7 vol% air, WHSV = 10 h^{-1}).

MoO_3 loading resulted in a decrease of the LA conversion and an increase of the PyA selectivity. For MT8, the overall selectivity of C2 products was the same as that for MT10, although also acetaldehyde was observed next to acetic acid. MT1 with the lowest MoO_3 loading was the most selective catalyst, reaching a PyA selectivity of about 90% at a LA conversion of 50%. Acetic acid was not observed for this catalyst. The by-products methylsuccinic anhydride and propionic acid are likely due to LA conversion on titania, as the data show that the yield of these by-products increased with increasing TiO_2 content. On the contrary, the selectivities towards oxidation products agree well with the MoO_3 content. These findings suggest that these side-reactions were catalyzed by bulk MoO_3 species present at higher Mo loading. The highest PyA yield of 60% was obtained using MT2 as the catalyst, which remains unchanged during 24 h on stream indicating the good stability of the MT2 catalyst (see the ESI†). The offline cumulative analysis of the liquid products reveals a carbon balance of 96%. The PyA yield of 60% is the highest reported for oxidative dehydrogenation of LA under mild reaction conditions.[21]

Based on the results presented above, we propose that the oxidative conversion of LA over the MoO_3/TiO_2 catalysts follows the reaction paths shown in Scheme 2. The dominant reaction is dehydrogenation of LA to PyA. The side-reactions include the further condensation of the PyA product with concomitant decarboxylation and dehydration to citraconic anhydride and methylsuccinic anhydride as well as the decarboxylation to CO_2 and acetaldehyde and the further oxidation of acetaldehyde to acetic acid.

3.3. Catalyst characterization

To gain further insight into the MoO_3/TiO_2 synergy, we characterized various materials. Fig. 3 shows the powder XRD patterns and UV-Raman spectra. The dominant diffraction features in the XRD patterns are related to the anatase form of titania. Characteristic diffraction features of crystalline MoO_3 were absent in MT1 and MT2. The other catalysts displayed clear (020) and (021) reflections of MoO_3, which became more intense and sharper at higher MoO_3 content. No diffraction peaks related to mixed oxide phases were observed.[35] All of the Raman spectra contained a broad band centered at around 790 cm^{-1}, which is attributed to the first overtone of the O–Ti–O vibration.[36] For the Mo-containing samples, additional bands in the 940–990 cm^{-1} region are due to different MoO_x species. The band at 942 cm^{-1} in MT1 is due to the isolated tetrahedral $[MoO_4]^{2-}$ species.[36] With increasing MoO_3 content, this band shifted to higher wavenumbers. These changes point to the agglomeration of Mo-oxides and an increasing amount of octahedral Mo species.[37–39] Oligomeric Mo-oxides are characterized by the Raman band at *ca.* 980 cm^{-1}, which was also observed for $Mo_7O_{24}^{6-}$ and $Mo_8O_{26}^{4-}$ clusters in solutions.[40] The band at 992 cm^{-1}, which appeared in the Raman spectrum of MT5 and which became more intense at higher MoO_3 content, is due to the Mo=O stretching vibration in Mo-oxide aggregates. Based on these results, it appears that the monolayer Mo-oxide coverage is reached between 2 wt% and 5 wt%. In a previous study, it was determined that the monolayer capacity of anatase is about 0.16 wt% MoO_3 per square meter of surface area.[41] Based on the surface area of the anatase titania support used in this study (11.7 $m^2\ g^{-1}$, ESI Table S1†), a MoO_3 monolayer coverage of 2 wt% is estimated, which explains the formation of bulk segregated molybdena phases above a MoO_3 loading of 2 wt%.

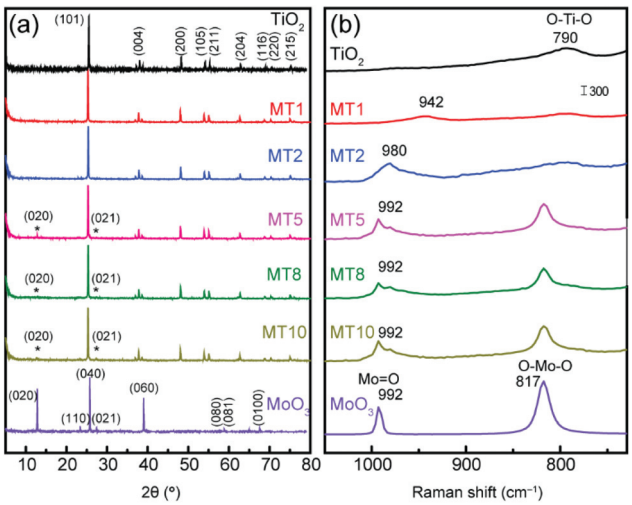

Fig. 3 (a) XRD patterns and (b) UV-Raman spectra for MoO_3, TiO_2, and MT catalysts.

Further evidence of the intimate contact between the components in the binary oxide catalysts is provided by TPR and UV-Vis spectroscopy. The corresponding data are shown in Fig. 4. Pure TiO_2 is hardly reducible at temperature below 900 °C. Pure MoO_3 shows three broad peaks with hydrogen uptake in the temperature range between 600 and 850 °C. According to Thomas *et al.*,[42] the first two main reduction features at 704 °C and 818 °C correspond to the reduction of MoO_3 to MoO_2 and further reduction of MoO_2 to the Mo^0 state, respectively. The small peak at 740 °C is attributed to the reduction of MoO_3 to Mo_4O_{11}. For MT catalysts, the first reduction step occurred at a much lower temperature than that for bulk MoO_3. Among them, MT2 shows the highest reducibility with the first reduction peak occurring already at 472 °C. The second reduction feature to metallic Mo occurred at the same temperature as that for MoO_3. The higher reducibility of the isolated surface Mo species implies a higher availability of oxygen species relevant to the removal of hydrogen atoms from lactic acid during its oxidative dehydrogenation.

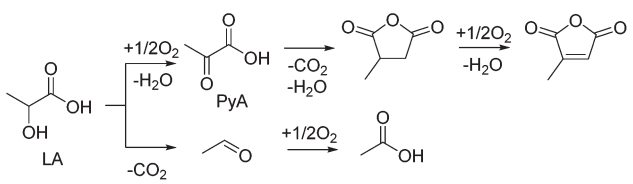

Scheme 2 The proposed reaction scheme for oxidative conversion of LA over MoO_3/TiO_2.

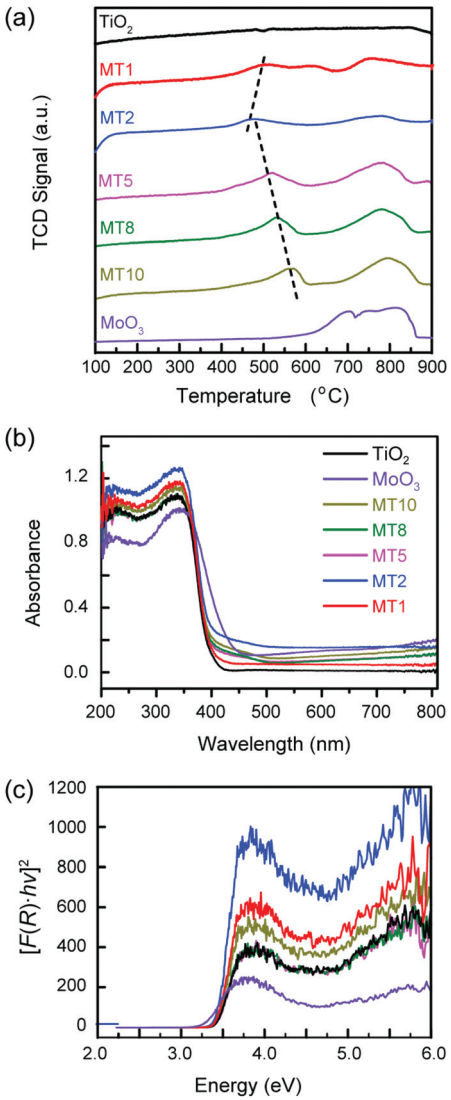

Fig. 4 (a) TPR traces, (b) UV-Vis absorption spectra and (c) corresponding Tauc plots for TiO_2, MoO_3 and MT catalysts.

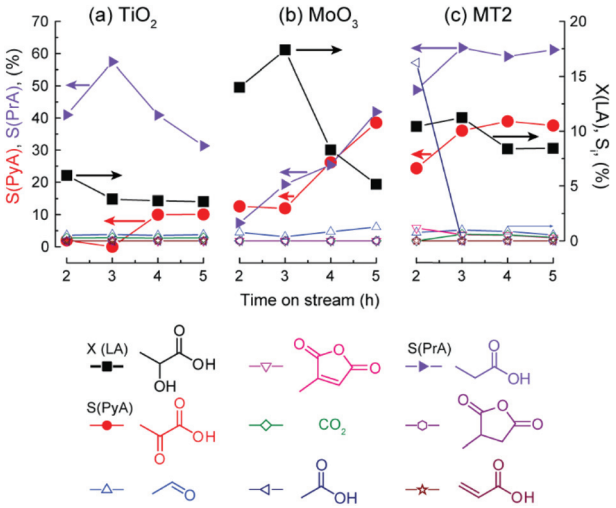

Fig. 5 Selectivities to PrA (propionic acid, right triangles, left *Y* axis), PyA (red circles, left *Y* axis), and to other minor products (open symbols, right axis) and LA conversion (black squares, right axis) under anaerobic conditions over (a) TiO_2, (b) MoO_3 and (c) MT2 (conditions: T = 200 °C, p = 1 atm, 4.0 vol% LA, 6.7 vol% N_2, WHSV = 10 h^{-1}).

According to Wachs and co-workers[43] the band-gap energy for the supported MoO_3 catalysts correlates with the Mo dispersion: isolated Mo-oxo species are characterized by a wider band gap. We recorded UV-Vis spectra and derived Tauc plots, depicted in Fig. 4b and c, respectively. Pure TiO_2 and MoO_3 have band gaps of 3.4 eV and 3.2 eV, respectively. For all MT catalysts, the band gap is shifted to higher energies. The highest band gap is observed for MT2 (Fig. 4c), further confirming the higher Mo dispersion.

3.4 Catalytic mechanism

In order to understand the mechanism better, we also carried out the conversion of LA without a gaseous oxidant. For this purpose, the reaction experiments were performed in a flow of nitrogen. The results are given in Fig. 5. TiO_2 provided low and stable LA conversion with a high selectivity (*ca.* 40%) to propionic acid (Fig. 5a). Pure MoO_3 initially showed a higher activity, but the conversion rapidly decreased with time on stream (Fig. 5b). The decrease in conversion was accompanied by a pronounced increase in the selectivities of PyA and propionic acid. Combinedly, these products made up about 80% of the products after 4 h on stream. The conversion was stable for MT2 (~10%) with a high selectivity to propionic acid (~60%), the remainder being PyA. We propose that the reaction in the absence of the external oxidant proceeds *via* a transfer hydrogenation mechanism, in which LA acts both as the hydrogen donor and the hydrogen acceptor. In the absence of an oxidant that can remove the proton and hydride from LA, hydrogenolysis is the dominant reaction, explaining why the propionic acid yield is higher than that of PyA. As propionic acid yield was higher with TiO_2 than that with MoO_3, we expect that the dehydrogenation and the associated hydrogenolysis reaction are catalyzed by the sites on the titania surface. The promoting role of MoO_3 is to provide mobile oxygen species, necessary for the removal of adsorbed H obtained by dehydrogenation of LA. The rapid deactivation of bulk MoO_3 in the absence of oxygen is associated with the reduction of the surface Mo sites in the course of the reaction.

This hypothesis about the role of Mo-oxide is supported by Mo 3d XPS spectra, which are compared in Fig. 6 for fresh and spent MT2 recovered after reaction with LA in air and nitrogen. The surface of the fresh MT2 catalyst contains Mo^{6+} and Mo^{5+} species in a 75 : 25 ratio. The spent catalysts contain a higher amount of reduced Mo species. The sample contained these species in a 65 : 35 ratio, showing that reduction of Mo-oxide species is part of the catalytic cycle. In the absence of oxygen, the extent of Mo reduction is significantly higher. The Ti 3d XPS spectra show that Ti is not reduced under the reaction conditions (ESI, Fig. S1†). Scanning electron micrographs show that the occurrence of line defects in spent bulk MoO_3

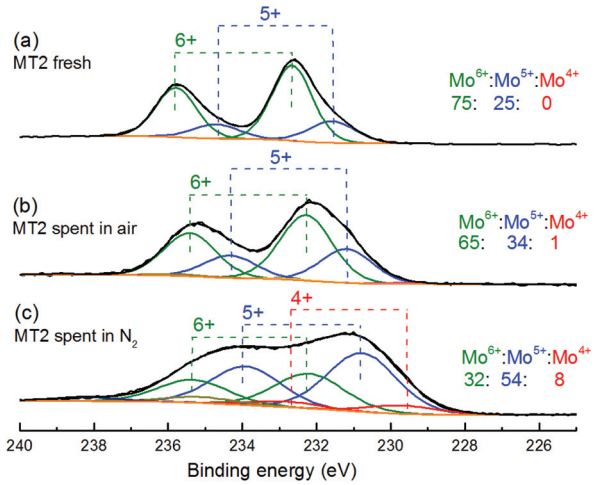

Fig. 6 Mo 3d binding energy region of XPS spectra of (a) fresh and spent MT2 following the reaction with LA in (b) air and (c) nitrogen. The displayed ratios of Mo oxidation states were obtained by deconvolution of the spectra.

(Fig. S2a and b†) is due to the removal of lattice oxygen on the MoO_3 surface. Such changes are expectedly absent for the spent TiO_2 sample (Fig. S2c–e†). The result that Mo-oxides are reduced is consistent with the XPS findings.

Previous studies have found that the redox and acid–base properties of metal oxide catalysts correlated well with their catalytic performance in selective oxidation reactions.[44–46] It has also been demonstrated that oxidative dehydrogenation of ethanol could be used as a model reaction to investigate the redox properties of V_2O_5/TiO_2 catalysts.[47] Inspired by these studies, we also applied ethanol oxidation as a model reaction to investigate these properties of the catalysts used for LA conversion. The catalytic results are summarized in Fig. 7. The acetaldehyde yield with TiO_2 is *ca.* 30% with very high acetaldehyde selectivity (*ca.* 99%). This confirms that TiO_2 is highly selective for oxidative dehydrogenation reaction. For MT2, the acetaldehyde yield reached the highest value of 93%. At higher loading, the yield decreased again. The best performance for MT is keeping with the high reducibility of MT2. For the bulk MoO_3 catalyst, a high acetaldehyde yield (~79%) was obtained, although the acetaldehyde selectivity was much lower than TiO_2. This is caused by the formation of diethyl ether by-product, which is catalyzed by acidic sites of the catalysts.[48,49] The formation of diethyl ether is only noticeable when the MoO_3 loading is higher than 1 wt% and with bulk MoO_3. The diethyl ether yield increased along with the MoO_3 loading, indicating an increase of the acidity with increasing MoO_3 loading content.

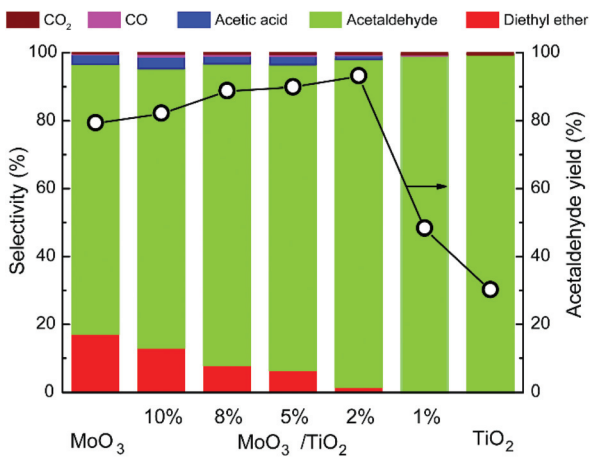

Fig. 7 Acetaldehyde yield (open circles) and product selectivities (bars) in the oxidation of ethanol over MoO_3, TiO_2 and MT catalysts after a 4 h time on stream (conditions: T = 300 °C, p = 1 atm, 1.5 vol% C_2H_5OH, 4.5 vol% O_2, balance He, GHSV = 100 000 mL g^{-1} h^{-1}).

Pyridine FT-IR was further applied to characterize the Lewis and Brønsted acidity of these catalysts (Fig. S3†). As expected, TiO_2 mainly contains Lewis acid sites giving absorption bands at 1450 cm^{-1} and 1480 cm^{-1}.[52,53] The loading of MoO_3 on TiO_2 introduced new Brønsted acid sites characterized by the bands at 1540 cm^{-1} and 1638 cm^{-1}. Consistently, these two bands are only noticeable for the bulk MoO_3 and MT catalysts with more than 1 wt% MoO_3 loading. The general trend also correlates well with the Raman results where oligomeric Mo species start to form when the MoO_3 loading is higher than 1 wt%. Therefore, it is reasonable to conclude that the oligomeric Mo species on the titania surface introduce more Brønsted acid sites that catalyze dehydration of ethanol and result in the formation of a diethyl ether side-product.[50,51] A high amount of Brønsted acid sites is also known to catalyze decarboxylation reactions[54–56] which explains the lower selectivity at higher MoO_3 content.

Scheme 3 shows tentative catalytic cycles for the aerobic and anaerobic conversion of LA by highly dispersed tetrahedral Mo sites located on the titania support. The first step in the oxidative dehydrogenation of LA (Scheme 3a) involves the coordination of LA to the catalyst surface by the reaction of basic OH groups of titania, forming lactate species ($CH_3CH(OH)COO$), which have earlier been identified by IR spectroscopy.[57] The next step is deprotonation of the secondary alcohol group in adsorbed lactate by the molybdate species, followed by hydride abstraction of the resulting activated lactate intermediate by the Mo center, which results in the reduction of Mo and the formation of pyruvate. Hydrolysis of the pyruvate adsorbed on the surface yields PyA and regenerates the basic OH group on the titania surface. After desorption of water, the Mo center is reduced to the +4 state. Molecular oxygen oxidizes the surface back to the +6 state. In the absence of oxygen, the removal of surface H species has to proceed *via* another pathway. Bimolecular transfer hydrogenation resulting in propionic acid as the major by-product in addition to the PyA product (Scheme 3b) requires synergy between Lewis acid and base sites.[58] The initial LA activation would involve dissociation of the carboxyl and hydroxyl groups to form a dual-site bound activated lactate species. Oxidation of the surface lactate species takes place either *via* hydride abstraction by the Lewis acid sites of titania (shown in Scheme 3b) or *via* a con-

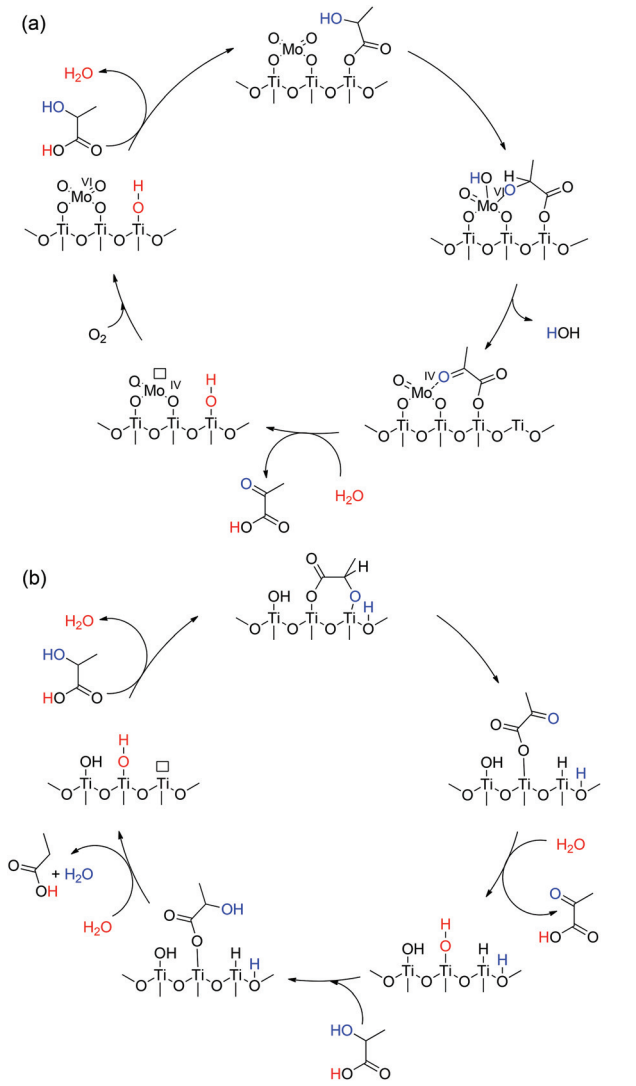

Scheme 3 Proposed catalytic reaction mechanisms for the (a) aerobic and (b) anaerobic conversion of LA over MoO_3/TiO_2 catalysts.

certed electron-coupled proton transfer.[59] Further *in situ* spectroscopy and computational modeling would be required to understand this mechanism. Hydrolysis of the resulting pyruvate adsorbates regenerates the basic OH group. This OH group activates another LA molecule to form a surface lactate, which then undergoes hydrogenolysis by reacting with the surface hydride and the proton with concomitant release of water and formation of a surface propionate. The latter can desorb after hydrolysis of its bond with the surface OH group.

4. Conclusions

We report that highly dispersed molybdate species on titania are active catalysts for the oxidative dehydrogenation of lactic acid to pyruvic acid. MoO_3, TiO_2 and physically mixed MoO_3–TiO_2 are selective catalysts themselves, but their activities are low compared to the binary oxide obtained by dispersing Mo on titania. The optimum catalyst is a 2 wt% MoO_3/TiO_2, in which tetrahedral Mo species predominate over oligomeric Mo-oxides. This catalyst provides pyruvic acid with the yield and selectivity of *ca.* 60% and 80%, respectively. The pyruvic acid productivity is 0.56 g g^{-1} h^{-1}. At higher MoO_3 content, the formation of oligomeric Mo-oxides leads to the formation of sites that catalyze undesired side-reactions such as decarboxylation to acetaldehyde, which can be further oxidized to acetic acid. XPS measurements indicate that surface redox processes of Mo are involved in the catalytic cycle. A mechanism is proposed, in which lactic acid adsorbs to basic sites of the titania surface and is then dehydrogenated over the vicinal Mo=O moiety of a tetrahedral Mo site. The catalytic cycle closes by hydrolysis of pyruvate and desorption of water accompanied by the reduction of the Mo site. The reduced Mo site is then re-oxidized by molecular oxygen to close the catalytic cycle. In the absence of oxygen, a less efficient catalytic cycle involving a bimolecular transfer self-hydrogenation process takes place. The reaction in this case results in the formation of propionic acid next to pyruvic acid as the primary product.

Acknowledgements

This work was performed in the framework of the European Union FP7 NMP project NOVACAM ("Novel Cheap and Abundant Materials for Catalytic Biomass Conversion", FP7-NMP-2013-EU-Japan-604319). E. A. P. thanks the Government of the Russian Federation (Grant 074-U01) for his personal professorship in the framework of the ITMO Fellowship and Professorship Program.

References

1 E. L. Kunkes, D. A. Simonetti, R. M. West, J. C. Serrano-Ruiz, C. A. Gärtner and J. A. Dumesic, *Science*, 2008, **322**, 417–421.
2 J. J. Bozell, *Science*, 2010, **329**, 522–523.
3 P. Maki-Arvela, I. L. Simakova, T. Salmi and D. Y. Murzin, *Chem. Rev.*, 2014, **114**, 1909–1971.
4 H. F. N. de Oliveira, C. Fares and R. Rinaldi, *Chem. Sci.*, 2015, **6**, 5215–5224.
5 J. David Rozzell, *US Patent* EP0135846A2, 1985.
6 D. H. Retief, B. E. Harris, E. L. Bradley and F. R. Denys, *J. Biomed. Mater. Res.*, 1985, **19**, 335–348.
7 H. Hayashi, S. Sugiyama, Y. Katayama, K. Sakai, M. Sugino and N. Shigemoto, *J. Mol. Catal.*, 1993, **83**, 207–217.
8 B. U. Kim, J. H. Baik, C. I. Oh, S. D. Lee, W. L. Kim and C. S. Yoo, *US Patent* US6183942B1, 2001.
9 E. Erlenmeyer, *Ber. Dtsch. Chem. Ges.*, 1881, **14**, 320–323.
10 J. W. Howard and W. A. Fraser, *Org. Synth.*, 1925, **4**, 63–64.
11 M. Ai and K. Ohdan, *Appl. Catal., A*, 1997, **150**, 13–20.
12 M. Ai, *Appl. Catal., A*, 2002, **234**, 235–243.
13 T. Tsujino, S. Ohigashi, S. Sugiyama, K. Kawashiro and H. Hayashi, *J. Mol. Catal.*, 1992, **71**, 25–35.

14 E. Heracleous, M. Machli, A. A. Lemonidou and I. A. Vasalos, *J. Mol. Catal. A: Chem.*, 2005, **232**, 29–39.
15 K. Chen, S. Xie, E. Iglesia and A. T. Bell, *J. Catal.*, 2000, **189**, 421–430.
16 K. Chen, S. Xie, A. T. Bell and E. Iglesia, *J. Catal.*, 2001, **198**, 232–242.
17 H. Hayashi, N. Shigemoto, S. Sugiyama, N. Masaoka and K. Saitoh, *Catal. Lett.*, 1993, **19**, 273–277.
18 T. Blasco and J. M. L. Nieto, *Appl. Catal., A*, 1997, **157**, 117–142.
19 E. V. Ramos-Fernandez, N. J. Geels, N. R. Shiju and G. Rothenberg, *Green Chem.*, 2014, **16**, 3358–3363.
20 K. Liu, A. Litke, Y. Su, B. G. van Campenhout, E. A. Pidko and E. J. M. Hensen, *Chem. Commun.*, 2016, **52**, 11634–11637.
21 S. Lomate, T. Bonnotte, S. Paul, F. Dumeignil and B. Katryniok, *J. Mol. Catal. A: Chem.*, 2013, **377**, 123–128.
22 H. Hayashi, N. Shigemoto, S. Sugiyama, N. Masaoka and K. Saitoh, *Catal. Lett.*, 1993, **19**, 273–277.
23 K. Brückman, B. Grzybowska, M. Che and J. M. Tatibouët, *Appl. Catal., A*, 1993, **96**, 279–288.
24 C. Brookes, M. Bowker and P. Wells, *Catalysts*, 2016, **6**, 92.
25 G. Tsilomelekis and S. Boghosian, *Phys. Chem. Chem. Phys.*, 2012, **14**, 2216–2228.
26 K. Chen, A. T. Bell and E. Iglesia, *J. Phys. Chem. B*, 2000, **104**, 1292–1299.
27 M. C. Abello, M. F. Gomez, M. Casella, O. A. Ferretti, M. A. Bañares and J. L. G. Fierro, *Appl. Catal., A*, 2003, **251**, 435–447.
28 D. Vanhove, S. R. Op, A. Fernandez and M. Blanchard, *J. Catal.*, 1979, **57**, 253–263.
29 M. Shetty, K. Murugappan, T. Prasomsri, W. H. Green and Y. Román-Leshkov, *J. Catal.*, 2015, **331**, 86–97.
30 G. Busca, L. Lietti, G. Ramis and F. Berti, *Appl. Catal., B*, 1998, **18**, 1–36.
31 A. N. Desikan, L. Huang and S. T. Oyama, *J. Chem. Soc., Faraday Trans.*, 1992, **88**, 3357–3365.
32 K. V. R. Chary, V. Vijayakumar and P. K. Rao, *Langmuir*, 1990, **6**, 1549–1550.
33 G. Ramis, G. Busca and V. Lorenzelli, *Z. Phys. Chem.*, 1987, **153**, 189–200.
34 T. Mallat and A. Baiker, *Chem. Rev.*, 2004, **104**, 3037–3058.
35 K. V. R. Chary, T. Bhaskar, K. K. Seela, K. Sri Lakshmi and K. R. Reddy, *Appl. Catal., A*, 2001, **208**, 291–305.
36 H. Hu, I. E. Wachs and S. R. Bare, *J. Phys. Chem.*, 1995, **99**, 10897–10910.
37 C. C. Williams, J. G. Ekerdt, J. M. Jehng, F. D. Hardcastle, A. M. Turek and I. E. Wachs, *J. Phys. Chem.*, 1991, **95**, 8781–8791.
38 M. R. Smith, L. Zhang, S. A. Driscoll and U. S. Ozkan, *Catal. Lett.*, 1993, **19**, 1–15.
39 G. C. Bond, S. Flamerz and L. van Wijk, *Catal. Today*, 1987, **1**, 229–243.
40 M. A. Vuurman and I. E. Wachs, *J. Phys. Chem.*, 1992, **96**, 5008–5016.
41 A. J. Van Hengstum, J. G. Van Ommen, H. Bosch and P. J. Gellings, *Appl. Catal.*, 1983, **5**, 207–217.
42 R. Thomas, E. M. van Oers, V. H. J. de Beer and J. A. Moulijn, *J. Catal.*, 1983, **84**, 275–287.
43 I. E. Wachs and B. M. Weckhuysen, *Appl. Catal., A*, 1997, **157**, 67–90.
44 J. C. Védrine and I. Fechete, *C. R. Chim.*, 2016, **19**, 1203–1225.
45 R. Schlögl, *Top. Catal.*, 2016, **59**, 1461–1476.
46 J. Janlamool and B. Jongsomjit, *Catal. Commun.*, 2015, **70**, 49–52.
47 V. V. Kaichev, Y. A. Chesalov, A. A. Saraev, A. Y. Klyushin, A. Knop-Gericke, T. V. Andrushkevich and V. I. Bukhtiyarov, *J. Catal.*, 2016, **338**, 82–93.
48 B. Grzybowska-Świerkosz, *Mater. Chem. Phys.*, 1987, **17**, 121–144.
49 A. Ouqour, G. Coudurier and J. C. Vedrine, *J. Chem. Soc., Faraday Trans.*, 1993, **89**, 3151–3155.
50 Q. Meng, H. Xin, Y. Zhang, Y. Huang, X. Yi, Y. Sun, S. Zhong and X. Li, *Sci. Adv. Mater.*, 2015, **7**, 2343–2351.
51 H. Xin, X. Li, Y. Fang, X. Yi, W. Hu, Y. Chu, F. Zhang, A. Zheng, H. Zhang and X. Li, *J. Catal.*, 2014, **312**, 204–215.
52 G. Busca, H. Saussey, O. Saur, J. C. Lavalley and V. Lorenzelli, *Appl. Catal.*, 1985, **14**, 245–260.
53 K. Tanaka and J. M. White, *J. Phys. Chem.*, 1982, **86**, 4708–4714.
54 C. Tang, J. Peng, X. Li, Z. Zhai, H. Gao, W. Bai, N. Jiang and Y. Liao, *Korean J. Chem. Eng.*, 2015, **33**, 99–106.
55 C. Tang, Z. Zhai, X. Li, L. Sun and W. Bai, *J. Catal.*, 2015, **329**, 206–217.
56 C. Tang, J. Peng, X. Li, Z. Zhai, W. Bai, N. Jiang, H. Gao and Y. Liao, *Green Chem.*, 2015, **17**, 1159–1166.
57 Y.-K. Chen, Y.-F. Lin, Z.-W. Peng and J.-L. Lin, *J. Phys. Chem. C*, 2010, **114**, 17720–17727.
58 T. Komanoya, K. Nakajima, M. Kitano and M. Hara, *J. Phys. Chem. C*, 2015, **119**, 26540–26546.
59 W. Karim, C. Spreafico, A. Kleibert, J. Gobrecht, J. VandeVondele, Y. Ekinci and J. A. van Bokhoven, *Nature*, 2017, **541**, 68–71.

